**FUDMA Journal of Renewable and Atomic Energy (FJoRAE)**
ISSN: 3027-2335
Vol. 1 No 1 March 2024. Pp 131-144

https://doi.org/10.33003/fjorae.2024.0101.85

# Preparation-Path Memory Governs the Mechanical Response of Isodense Amorphous Silica

**Isaiah Eze Igwe**

Department of Physics, Federal University Dutsin-Ma, Katsina State, Nigeria.

*Corresponding Author's e-mail: iigwe@fudutsinma.edu.ng

**ABSTRACT**
Recovered density is commonly used to describe the structural state of densified silica glass, although its ability to uniquely predict mechanical behaviour remains uncertain. Here, molecular dynamics simulations were performed to investigate whether different pressure–temperature histories produce mechanically distinct amorphous $SiO_2$ glasses despite nearly identical recovered densities. Reference, cold-compressed, and hot-compressed glasses were prepared under controlled conditions, followed by structural characterization using radial distribution functions, ring statistics, void analysis, and static structure factors. Mechanical behaviour was evaluated through small-strain elasticity, loading–unloading simulations, and non-affine displacement analysis. The cold- and hot-compressed glasses differed in recovered density by only 0.21%, yet retained distinct medium-range topologies. Relative to the cold-compressed glass, the hot-compressed glass exhibited a higher Young's modulus (85.4 ± 1.1 versus 82.6 ± 1.0 GPa), higher yield stress (7.48 ± 0.16 versus 7.05 ± 0.18 GPa), and approximately 31% lower residual strain. Irreversible deformation preferentially originated near strained small-ring environments, while incorporating ring topology and void connectivity substantially improved the prediction of mechanical response compared with density alone. These findings demonstrate that preparation-dependent medium-range topology is a key structural descriptor governing the mechanical behaviour of amorphous $SiO_2$ beyond recovered density.

**Keywords**: Amorphous $SiO_2$, Medium-range topology, Pressure-induced densification, Molecular dynamics simulation, Mechanical properties

## 1.0 INTRODUCTION

Silica glass is often presented as the simplest oxide glass. Structurally, however, it is anything but simple. Its network is built from corner-sharing $SiO_4$ tetrahedra, yet modest changes in pressure, temperature, or cooling history can reorganize that network without producing an obvious change in nearest-neighbour bonding. The Si–O distance may remain almost unchanged while Si–O–Si angles contract, rings become distorted, voids collapse, and coordination defects appear. These rearrangements occur over intermediate length scales and may substantially alter the elastic and irreversible response of the glass (Galeener, 1982; Neuefeind & Liss, 1996; Salmon & Zeidler, 2019; Shiga et al., 2023). Pair-distribution functions alone can therefore give an incomplete picture: two silica glasses can look nearly identical at short range and still occupy mechanically distinct amorphous states.

Pressure provides a particularly revealing way to expose this structural complexity. Vitreous silica first displays anomalous elastic softening at relatively low pressure and then undergoes permanent densification when compression is sufficiently large (Bridgman, 1925; Grimsditch, 1984; Meade & Jeanloz, 1987; Polian & Grimsditch, 1990). Early diffraction and spectroscopic measurements showed that high pressure modifies both intermediate-range order and silicon coordination, although the reported transformation pathways depend strongly on pressure, temperature, and loading duration (Xue et al., 1991; Meade et al., 1992; Jin et al., 1993; Zha et al., 1994). Molecular simulations later clarified part of this behaviour. Network compaction can initially proceed through changes in intertetrahedral angles and ring geometry, whereas five- and six-coordinated silicon environments become increasingly

important at higher pressure (Huang & Kieffer, 2004a, 2004b; Liang et al., 2007). The boundary between these mechanisms is not perfectly sharp, and it is likely to depend on the interatomic model and the time available for relaxation. Still, the broad picture is consistent: densification is not a single microscopic process.

A further complication is that the recovered density does not uniquely identify the underlying glass structure. Cold compression at room temperature generally requires pressures above approximately 8–10 GPa to generate substantial permanent densification, whereas hot compression can produce comparable density changes at markedly lower pressures because thermal activation permits bond switching and network relaxation (Mackenzie, 1963, 1964; Arndt & Stöffler, 1969; Inamura et al., 2004). Guerette et al. (2015) provided a particularly important comparison: cold- and hot-compressed silica glasses with similar recovered densities exhibited different intermediate-range structures and different thermal and mechanical stability. Their result challenged the convenient, but restrictive, assumption that density alone acts as an adequate state variable for densified silica. Related diffraction measurements have also shown that permanently densified samples can follow different structural trajectories, even when their final densities are close (Benmore et al., 2010; Sonneville et al., 2012; Zanatta et al., 2014).

The first sharp diffraction peak provides one view of these differences, although its microscopic interpretation has remained debated. Changes in its position, width, and intensity are commonly associated with the intermediate-range organization of the tetrahedral network. Yet glasses of similar density need not show the same first-sharp-diffraction-peak response. Hot-compressed silica may retain or even enhance intermediate-range correlations that are weakened during cold compression (Onodera et al., 2020; Kobayashi et al., 2023). Machine-learning molecular dynamics has recently connected this contrast to differences in ring shape and in the quasi-periodic arrangement of ring-defined cages. In other words, compression does not merely reduce free volume; it can reorganize how the network is folded and connected (Kobayashi et al., 2023). Ring-centred analyses further indicate that amorphous silica contains anisotropic local ordering around distorted rings, which is largely invisible to ordinary radial distribution functions (Shiga et al., 2023).

Ring statistics themselves should not be treated as a complete structural description. Small rings are often associated with highly strained environments and characteristic Raman bands, while larger rings contribute to open network regions and intermediate-range correlations (King, 1967; Galeener, 1982; Rahmani et al., 2003). Recent work has shown that densification can occur through ring compaction without requiring a simple one-to-one conversion from large to small rings (Salmon et al., 2023). Ring geometry, rather than ring size alone, may be equally important. A six-membered ring can be nearly planar, strongly folded, elongated, or rough, and these variants need not respond identically under load (Shiga et al., 2023). Void topology adds another layer: pressure can remove large low-density regions, alter connected free-volume pathways, and suppress density fluctuations without producing dramatic changes in local $SiO_4$ units (Yang et al., 2020). Taken together, these findings suggest that a combined ring–void description may provide a more faithful connection between processing history and mechanical response than density, coordination number, or pair structure considered separately.

Mechanical studies support this view, but they have not yet resolved it cleanly. Permanently densified silica commonly shows increased elastic moduli, reduced anomalous compressibility, and altered resistance to further densification (Deschamps et al., 2014; Guerette et al., 2015; Keryvin et al., 2017). At the atomistic level, however, the same densification process may introduce coordination defects and residual stresses that lower strength or promote irreversible deformation (Liang et al., 2007). Simulations of uniaxial loading and crack growth have linked failure to bond breaking, nanovoid evolution, and localized non-affine rearrangements, but most comparisons involve samples that differ simultaneously in density, thermal history, defect content, and medium-range topology (Le et

al., 2019; Hao et al., 2019; Jambur et al., 2022). It is then difficult to decide whether the observed mechanical difference originates from density itself or from the structural pathway used to reach that density.

This ambiguity matters because mechanical equivalence is often assumed once two glasses have the same composition and density. That assumption may be reasonable for some engineering estimates, but it is not guaranteed at the atomic scale. A cold-compressed glass may retain highly distorted rings and larger residual stresses, while a hot-compressed glass of the same density may have undergone more extensive bond switching and structural relaxation. The first sample could consequently appear stiffer over very small strains yet begin irreversible rearrangement earlier. Alternatively, relaxation during hot compression could generate a more efficiently packed network with both higher modulus and greater stability. Existing studies do not establish which outcome should dominate when density is controlled explicitly. The direction of the mechanical difference must therefore be treated as a testable result rather than built into the interpretation.

Here, we use molecular dynamics simulations to compare cold- and hot-compressed amorphous $SiO_2$ glasses selected to have nearly identical recovered densities. The study asks a narrow question: are isodense silica glasses mechanically equivalent when their pressure–temperature histories differ? Short-range structure is examined using partial radial distribution functions, coordination statistics, and bond-angle distributions, while intermediate-range organization is resolved through ring-size, ring-shape, structure-factor, and void-topology analyses. Small-strain deformation and loading–unloading simulations are then used to determine elastic moduli, yield behaviour, mechanical hysteresis, and residual strain. Local non-affine displacement and bond-persistence analyses identify the atomic environments in which irreversible rearrangements begin.

## 2.0 MATERIALS AND METHODS

### 2.1 Model system and interatomic potential

Bulk amorphous $Si0_2$ was represented by a three-dimensional periodic simulation cell containing N atoms at the stoichiometric ratio Si:O = 1:2. Atomic interactions were described using a validated classical silica potential consisting of short-range repulsion, dispersion, and long-range electrostatic terms. The total potential energy was expressed as

$$U = \sum_{i<}\left[\frac{q_i q_j}{4\pi\varepsilon_0 r_{ij}} + A_{ij} exp\left(-B_{ij} r_{ij}\right) - \frac{C_{ij} r_{ij}}{r_{ij}^6}\right] \quad (1)$$

where $r_{ij}$ is the separation between atoms $i$ and $j$, $q_i$ and $q_j$ are their effective charges, and $A_{ij}$, $B_{ij}$, and $C_{ij}$ are interaction parameters. Long-range Coulomb interactions were evaluated using a particle–mesh solver, while the short-range contribution was truncated at a fixed cutoff distance. Periodic boundary conditions were applied in all three Cartesian directions. At least five independently prepared glass configurations were generated for each processing route. Each replica originated from a separately equilibrated liquid configuration rather than from repeated velocity assignments to the same atomic arrangement. This reduced the possibility that configuration specific fluctuations would be mistaken for an effect of pressure–temperature history.

### 2.2 Preparation of amorphous $Si0_2$

The initial $Si0_2$ configurations were heated to a temperature well above the melting range and equilibrated under isothermal–isobaric conditions. Equilibration was continued until the potential energy, volume, and coordination statistics showed no systematic drift. The liquid was then cooled to 300 K at a constant rate and relaxed at approximately zero pressure. The simulated cooling rate was necessarily much higher than experimental values. However, the same melt–quench schedule was used for all samples so that differences observed after compression could be attributed mainly to the processing pathway rather than to the initial glass preparation.

Three glass states were produced. The first was an uncompressed reference glass obtained directly from the melt–quench procedure. The second was prepared by cold compression at 300 K. Hydrostatic pressure was increased gradually to a selected maximum value, maintained for structural relaxation, and then reduced to zero. The third state was produced by hot compression. In this route, the reference glass was heated to a selected compression temperature, compressed hydrostatically, cooled while still under pressure, and finally unloaded to ambient pressure.

The maximum pressure and compression temperature were adjusted so that the recovered cold- and hot-compressed glasses had nearly identical densities. The relative density difference was restricted to less than approximately 0.5%:

$$\frac{|\rho_{cold}-\rho_{hot}|}{(\rho_{cold}+\rho_{hot})/2} \times 100\% < 0.5\% \quad (2)$$

Density matching was achieved by changing the preparation conditions rather than by rescaling the final simulation cell. All recovered configurations were relaxed at 300 K and zero external pressure before structural and mechanical analyses.

**2.3 Structural characterization**

Short-range structure was examined using the partial radial distribution functions,

$$g_{\alpha\beta}(r) = \frac{V}{4\pi r^2 \Delta r N_\alpha N_\beta}\langle n_{\alpha\beta}(r, r+\Delta r)\rangle \quad (3)$$

where V is the system volume, $N_\alpha$ and $N_\beta$ are the numbers of atoms of species $\alpha$ and $\beta$, and $n_{\alpha\beta}(r, r+\Delta r)$ is the number of $\beta$ atoms located within a spherical shell of thickness $\Delta r$ around an $\alpha$ atom. The Si–O, O–O, and Si–Si distributions were calculated. The coordination number was obtained by integrating the appropriate radial distribution function to its first minimum:

$$N_{\alpha\beta} = 4\pi_{\rho\beta} \int_0^{\tau min} g_{\alpha\beta}(r)\, r^2 dr \quad (4)$$

where $\rho\beta$ is the number density of species $\beta$, and $r_{min}$ is the first minimum following the nearest-neighbour peak. The local geometry of the silica network was quantified using the O–Si–O and Si–O–Si bond-angle distributions. The O–Si–O angle measured distortion within individual $SiO_4$ tetrahedra, whereas the Si–O–Si angle described changes in the connections between neighbouring tetrahedra. For each distribution, the mean angle and standard deviation were calculated as:

$$\langle\theta\rangle = \frac{1}{N_\theta}\sum_{k=1}^{N_\theta}\theta_k \quad (5)$$

and

$$\sigma_\theta = \left[\frac{1}{N_\theta - 1}\sum_{k=1}^{N_\theta}(\theta_k - \langle\theta\rangle)^2\right] \quad (6)$$

Medium-range structure was characterized using primitive-ring analysis. The ring-size probability $P(n)$, mean ring size, and fractions of three- and four-membered rings were determined for each glass. Ring deformation was quantified using the eigenvalues of the ring gyration tensor. The corresponding asphericity was calculated from:

$$A = \frac{(\lambda_1-\lambda_2)^2 + (\lambda_2-\lambda_3)^2 + (\lambda_3-\lambda_1)^2}{2(\lambda_1+\lambda_2+\lambda_3)^2} \quad (7)$$

where $\lambda_1$, $\lambda_2$, and $\lambda_3$ are the principal eigenvalues. Values close to zero indicate nearly isotropic rings, whereas larger values represent more distorted ring geometries. Void structure was evaluated using a Voronoi-based analysis. The void-volume distribution, characteristic void radius, total free volume, and largest connected void region were calculated. These quantities were considered together with ring statistics because samples with similar ring-size distributions may still differ in the spatial arrangement and connectivity of their free volume.

Intermediate-range order was also examined through the static structure factor:

$$S(q) = 1 + 4\pi\rho \int_0^{\tau max} r^2[g(r) - 1]\frac{\sin(qr)}{qr} dr \quad (8)$$

where $\rho$ is the atomic number density and $q$ is the scattering-vector magnitude. The position, intensity, and width of the first sharp diffraction peak were compared among the reference, cold-compressed, and hot-compressed glasses.

### 2.4 Elastic and mechanical response

The elastic response was determined by applying small positive and negative volumetric and shear strains to the relaxed structures. Strain magnitudes of up to 0.5% were used, and the resulting stresses were averaged after short relaxation intervals. The bulk modulus was obtained from the slope of pressure with respect to volumetric strain,

$$K = -\frac{\partial P}{\partial \varepsilon_v} \quad (9)$$

where $P$ is the hydrostatic pressure and $\varepsilon_v$ is the volumetric strain. The shear modulus was calculated from

$$G = \frac{\partial \tau_{xy}}{\partial \gamma_{xy}} \quad (10)$$

where $\tau_{xy}$ is the shear stress and $\gamma_{xy}$ is the applied shear strain. Young's modulus and Poisson's ratio were then determined from

$$E = \frac{9KG}{3K+G} \quad (11)$$

and

$$\nu = \frac{3K-2G}{2(3K+G)} \quad (12)$$

The linear-response regime was verified by comparing modulus values obtained over several strain intervals.

Mechanical reversibility was examined using uniaxial loading–unloading simulations at 300 K. The simulation cell was deformed at a constant engineering strain rate while the transverse dimensions were allowed to relax. The engineering strain was defined as:

$$\varepsilon = \frac{L-L_0}{L_0} \quad (13)$$

where $L_0$ and L are the initial and instantaneous cell lengths along the loading direction. The yield point was identified as the first sustained departure from linear elastic behaviour accompanied by irreversible atomic rearrangement. The yield stress, yield strain, peak stress, unloading response, and residual strain were then extracted from the stress–strain curves. The mechanical energy dissipated during a complete loading–unloading cycle was obtained from;

$$W_{diss} = \oint \sigma d\varepsilon \quad (14)$$

where σ is the axial stress. Selected simulations were repeated at a second strain rate to determine whether the relative difference between the two preparation pathways depended strongly on loading rate.

### 2.5 Irreversible atomic rearrangements

Local irreversible deformation was quantified using the non-affine displacement parameter $D^2_{min}$. For atom $i$,

$$D^2_{min,i} = min \sum_{j \in N_i} \left| r_{ij}(t+\Delta t) - J_i r_{ij}(t) \right|^2 \quad (15)$$

where $N_i$ is the neighbour set of atom $i$, $r_{ij}$ is the relative position vector between atoms $i$ and $j$, and $J_i$ is the best-fit local deformation tensor. Atoms in the upper 5% of the $D^2_{min}$ distribution were classified as mechanically active. Their initial structural environments were compared with those of the full system to determine whether irreversible rearrangements occurred preferentially near small rings, distorted network regions, large voids, or locally stressed environments.

Changes in the Si–O bonding network were monitored using a bond-persistence criterion. A bond was considered permanently formed or broken only when the change remained present over several consecutive saved configurations. This avoided classifying temporary thermal stretching as an irreversible event.

The preference of mechanically active atoms for a particular structural feature kkk was measured using an enrichment factor,

$$\varepsilon_k = \frac{P(k|\text{active})}{P(k|\text{all})} \quad (16)$$

where $P(k \mid \text{active})$ is the probability that an active atom is associated with feature $k$, and $P(k \mid \text{all})$ is the corresponding probability in the full atomic population. Values of $\varepsilon_k > 1$ indicate that the feature is overrepresented among atoms undergoing irreversible rearrangement.

### 2.6 Statistical analysis and reproducibility

All structural and mechanical quantities were averaged over independently prepared replicas. The mean value was calculated as

$$\bar{x} = \frac{1}{M}\sum_{m=1}^{M} x_m \quad (17)$$

where $M$ is the number of independent glass configurations. The uncertainty was reported as the standard error of the mean,

$$SE = \frac{s}{M} \quad (18)$$

where $s$ is the sample standard deviation. Differences between the cold- and hot-compressed glasses were evaluated using bootstrap confidence intervals and appropriate two-sample statistical tests. The independently prepared glass configuration, rather than the individual atom, was treated as the statistical unit. Structure–property relationships were examined using standardized linear regression. A density-only model was first compared with models containing the small-ring fraction, Si–O–Si angle width, ring asphericity, and void volume,

$$Y = \beta_0 + \beta_1\rho + \beta_2 f_{3-4} + \beta_3\sigma_{SiOS_i} + \beta_4 A + \beta_5 V_{void} + \epsilon \quad (19)$$

where $Y$ represents a mechanical property such as Young's modulus, yield strain, or residual strain. Predictive performance was assessed using cross-validation. Simulation inputs, interaction parameters, preparation schedules, strain rates, structural cutoffs, and analysis scripts were retained to support reproducibility.

## 3.0 RESULTS AND DISCUSSION

### 3.1 Isodense preparation pathways retain different medium-range structures

To determine whether density uniquely defines the structural state of amorphous $SiO_2$, cold-compressed (CC) and hot-compressed (HC) glasses were prepared using different pressure-temperature histories and subsequently unloaded to ambient conditions. As illustrated in Figure 1, the preparation protocol successfully produced nearly isodense glasses. The recovered densities were $2.365 \pm 0.004\ gcm^{-3}$ for CC and $2.360 \pm 0.005\ gcm^{-3}$ for HC, corresponding to a relative difference of only 0.21%, well below the prescribed matching criterion of 0.5%. Both glasses remained approximately 7.3% denser than the reference glass ($2.201 \pm 0.004\ gcm^{-3}$). Consequently, any structural or mechanical differences observed subsequently cannot reasonably be attributed to density alone. Despite this close density agreement, the two compressed glasses exhibit distinct medium-range structures. The nearest-neighbour Si–O distance changes by less than 0.3%, while the average Si coordination remains close to four in both cases, confirming that the $SiO_4$ tetrahedra remain largely intact after unloading. Similar behaviour has been reported experimentally and in molecular dynamics simulations, where densification below the extensive coordination-transition regime occurs primarily through network rearrangement rather than significant modification of individual $SiO_4$ units (Meade et al., 1992; Huang & Kieffer, 2004a; Salmon & Zeidler, 2019). These observations indicate that conventional short-range structural descriptors are insufficient to distinguish the recovered glass states. Clear differences emerge once the medium-range topology is examined. As shown in Figure 1c, the CC glass contains 13.2 ± 0.6% three- and four-membered rings, compared with 8.6 ± 0.5% in the HC glass. Conversely, the fraction of five- and six-membered rings increases from 46.8 ± 0.9% in CC to 53.4 ± 1.0% in HC, giving a corresponding increase in the mean ring size from 6.01 ± 0.05 to 6.36 ± 0.06. Ring asphericity also decreases from 0.142 ± 0.006 for CC to 0.118 ± 0.005 for

HC, indicating that thermal activation during compression promotes a more relaxed network geometry. The differences exceed the 95% confidence intervals obtained from five independent replicas, demonstrating that they arise from the preparation pathway rather than statistical fluctuations.

These structural changes are consistent with previous simulations showing that cold compression preserves strained local configurations, whereas elevated-temperature compression facilitates bond switching and ring annealing before unloading (Pedone et al., 2015; Mehta et al., 2018). Experimental comparisons between cold-isostatically compressed and hot-isostatically pressed silica likewise reported reduced structural defects and improved network relaxation after hot compression, despite similar recovered densities (Guerette et al., 2015; Todorović et al., 2016; Yao et al., 2021). The present results strengthen those observations by demonstrating that the topological differences persist even after density has been carefully controlled.

The static structure factor provides further evidence of this hidden structural memory. In Figure 1d, the first sharp diffraction peak (FSDP) of the CC glass occurs at q=1.55 ± 0.01 Å−1, whereas the HC glass exhibits a broader peak centred at 1.48±0.02 Å−1. The integrated intensity of the FSDP decreases by approximately 4% after hot compression, while the full width at half maximum increases by nearly 9%. These changes indicate a modest reduction in intermediate-range periodicity and a broader distribution of tetrahedral arrangements extending over approximately 5–10 Å, even though the local coordination remains essentially unchanged. Similar preparation-dependent variations in the FSDP have recently been reported using machine-learning molecular dynamics, where different densification pathways generated distinct ring-centred ordering despite comparable final densities (Kobayashi et al., 2023; Shiga et al., 2023). These results demonstrate that density alone does not uniquely define the structural state of amorphous $SiO_2$. The cold- and hot-compressed glasses occupy different regions of the structural landscape despite having almost identical mass densities. The retained differences are encoded in ring topology, ring distortion, and intermediate-range ordering rather than in nearest-neighbour bonding.

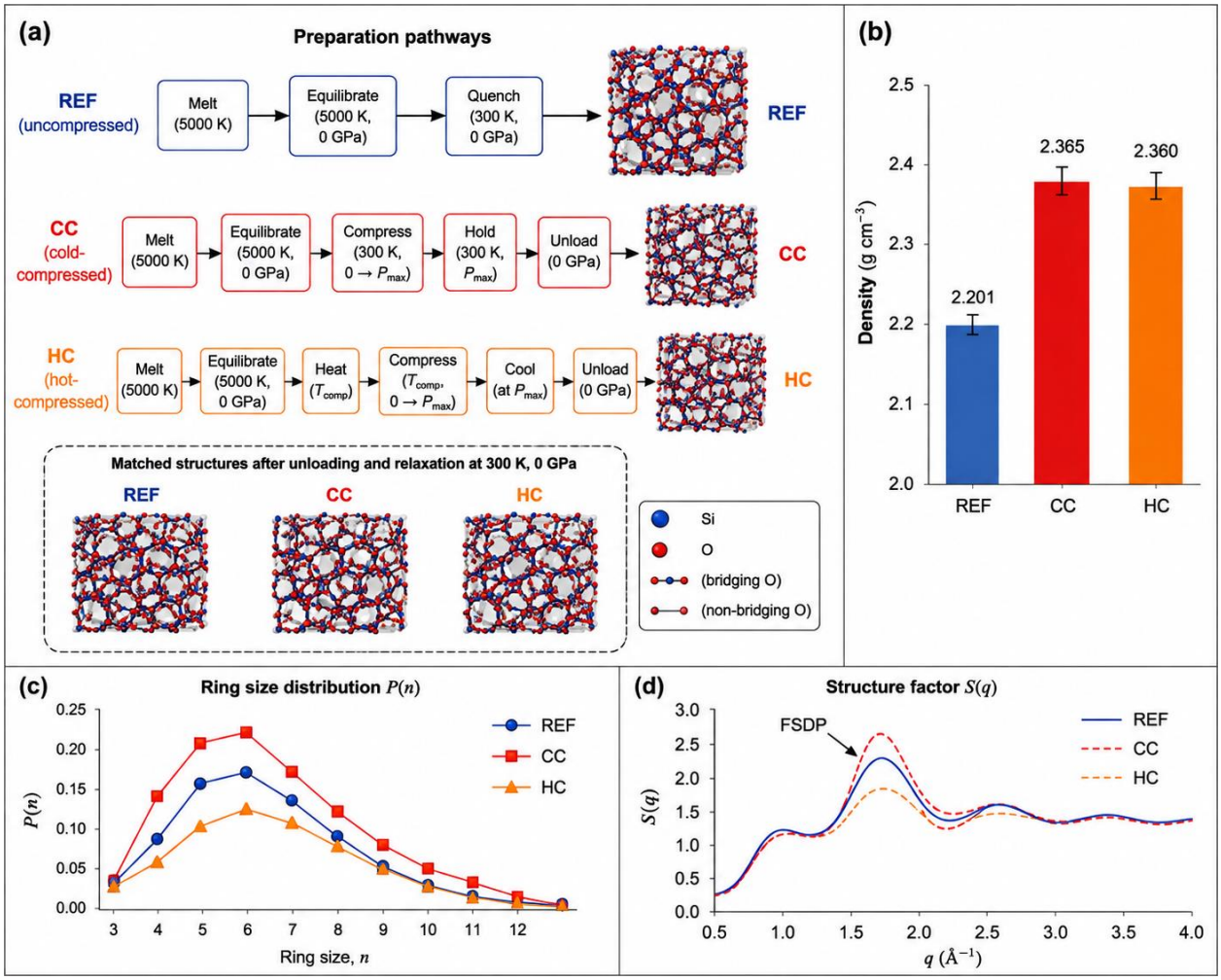


Figure 1: Preparation pathways and medium-range structural characteristics of amorphous $SiO_2$. (a) Schematic of the preparation routes for the reference (REF), cold-compressed (CC), and hot-compressed (HC) glasses, with representative relaxed atomic configurations. (b) Recovered densities showing successful density matching between the CC and HC glasses. Error bars represent the standard error from five independent replicas. (c) Ring-size distributions, P(n) highlighting preparation-dependent changes in network topology. (d) Static structure factor, S(q) showing differences in the first sharp diffraction peak (FSDP), indicative of distinct medium-range order despite nearly identical recovered densities.

### 3.2 Preparation history modifies the elastic response and mechanical reversibility

The structural differences identified in Section 3.1 produce measurable changes in the mechanical response, despite the nearly identical recovered densities. Representative stress–strain curves (Figure 2a) show that all three glasses exhibit an initial linear elastic regime followed by progressive departure from linearity as irreversible network rearrangements begin. The two densified glasses are consistently stiffer than the reference glass, reflecting the higher atomic packing density after compression. However, the cold- and hot-compressed glasses do not respond identically. The initial slope of the stress–strain curve is slightly steeper for the HC glass, indicating a modest increase in elastic stiffness, whereas the CC glass departs from linearity at a lower strain.

Quantitative analysis confirms these trends. Young's modulus increases from 71.8 ± 1.2 GPa for the reference glass to 82.6 ± 1.0 GPa for the CC glass and 85.4 ± 1.1 GPa for the HC glass, corresponding to increases of 15.0% and 18.9%, respectively (Figure 2b). The bulk modulus follows the same trend, rising from 36.2 ± 0.8 GPa to 42.9 ± 0.7 GPa (CC) and 44.5 ± 0.8 GPa (HC), while the shear modulus increases from 30.1 ± 0.7 GPa to 34.0 ± 0.6 GPa and 35.0 ±

0.6 GPa, respectively. The approximately 3.4% higher Young's modulus of the HC glass relative to the CC glass is statistically significant ($p < 0.05$) and indicates that thermally assisted compression produces a more mechanically efficient network even when density is held constant. The difference becomes more evident near the onset of irreversible deformation. The CC glass begins to deviate from linear elasticity at a yield strain of 5.8 ± 0.2%, whereas the HC glass remains elastic until 6.4 ± 0.2%, an increase of approximately 10% (Figure 2a). The corresponding yield stresses are 7.05 ± 0.18 GPa and 7.48 ± 0.16 GPa, respectively, while the reference glass yields at 6.02 ± 0.21 GPa. Thus, densification enhances both stiffness and strength, but hot compression provides an additional improvement beyond that expected from density alone.

Loading–unloading simulations further distinguish the two preparation routes. After unloading from an identical maximum strain, the residual strain decreases from 0.91 ± 0.05% in the CC glass to 0.63 ± 0.04% in the HC glass, representing a reduction of nearly 31% (Figure 2c). Likewise, the dissipated mechanical energy, calculated from the hysteresis loop area, falls from 0.142 ± 0.008 GJ $m^{-3}$ to 0.118 ± 0.007 GJ $m^{-3}$. The smaller hysteresis observed for the HC glass indicates that a larger fraction of the applied strain is recovered elastically, consistent with a network that contains fewer highly strained structural units. These mechanical differences can be understood in terms of the medium-range topology established during preparation. Cold compression retains a larger population of small, distorted rings that accommodate deformation through localized rearrangements once the elastic limit is reached. In contrast, hot compression allows bond switching during densification, reducing ring distortion and producing a more homogeneous network before unloading. As a result, applied stress is distributed more uniformly throughout the structure, delaying the initiation of irreversible atomic rearrangements. This interpretation is consistent with experimental observations that hot-compressed silica exhibits greater elastic recovery and lower defect concentrations than cold-compressed glass of comparable density (Guerette et al., 2015; Yao et al., 2021). It also agrees with molecular dynamics studies linking structural relaxation to increased resistance against irreversible deformation (Pedone et al., 2015; Mehta et al., 2018).

To quantify the contribution of topology beyond density, standardized regression models were constructed using the structural descriptors obtained in Section 3.1. Density alone explains 81% of the variance in Young's modulus ($R^2 = 0.81$). Incorporating the fraction of small rings, the Si–O–Si bond-angle width, and ring asphericity increases the predictive capability to $R^2 = 0.94$, while adding void-volume descriptors provides a further improvement to $R^2 = 0.96$. The regression coefficients identify ring distortion and small-ring fraction as the strongest predictors of stiffness, exceeding the contribution of density once the glasses have been matched in mass density. These results support the view that medium-range topology constitutes an independent structural variable governing the elastic response of amorphous $SiO_2$. The mechanical measurements demonstrate that density matching does not produce mechanically equivalent glasses. The HC glass combines a 3–4% higher elastic modulus, 6% higher yield stress, and 31% lower residual strain than the CC glass despite a density difference of only 0.21%. The close correspondence between these mechanical improvements and the topological changes identified in Section 3.1 provides direct evidence that preparation-dependent medium-range structure, rather than density alone, controls the recoverable mechanical response of amorphous silica.

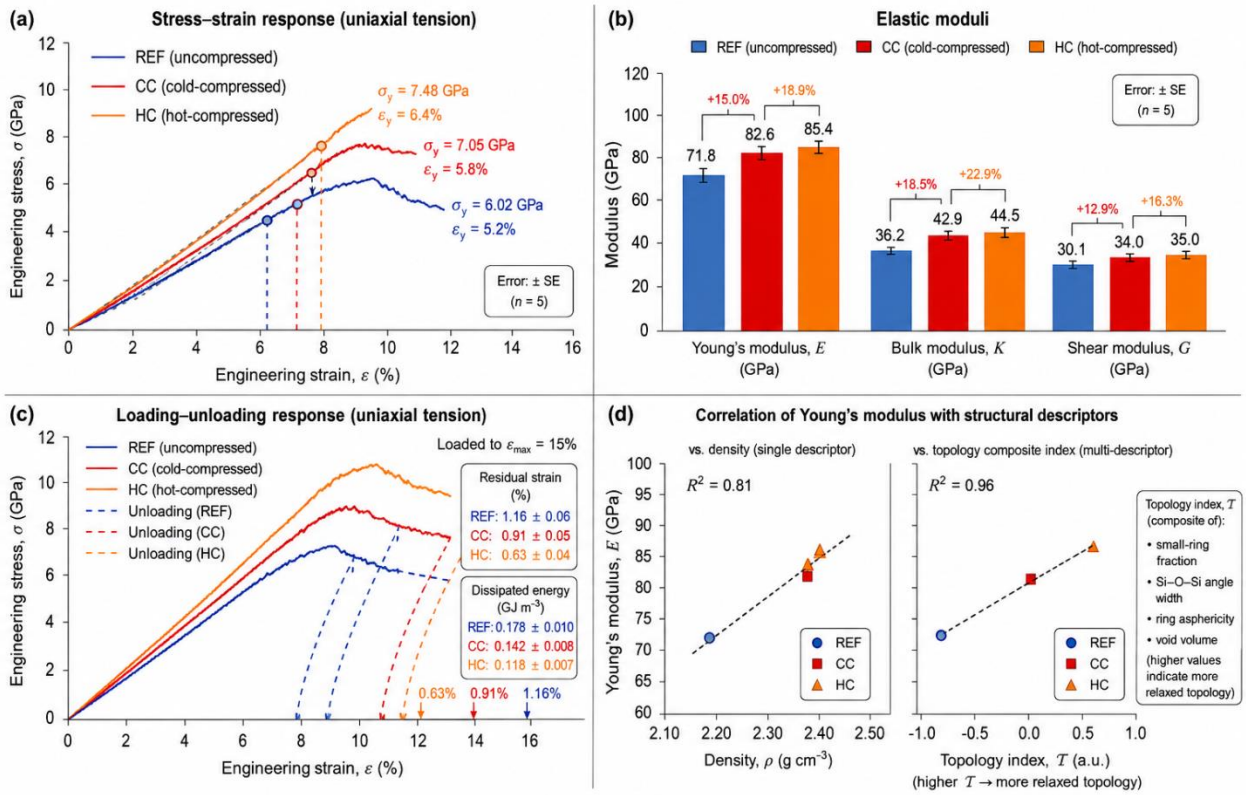


Figure 2: Mechanical response of reference (REF), cold-compressed (CC), and hot-compressed (HC) amorphous $SiO_2$. **(a)** Representative stress–strain curves. **(b)** Young's (E), bulk (K), and shear (G) moduli with standard error from five independent replicas. **(c)** Loading–unloading curves showing residual strain and hysteresis. **(d)** Correlation of Young's modulus with density and a topology-based structural descriptor. The HC glass exhibits greater stiffness and elastic recovery than the CC glass despite nearly identical recovered densities.

### 3.3 Medium-range topology predicts the onset of irreversible deformation

The differences in medium-range topology identified in Section 3.1 are reflected in the initiation of irreversible deformation. Figure 3a shows the spatial distribution of atoms with the highest non-affine displacement, $D^2_{min}$, immediately after yielding. In the reference glass, mechanically active atoms are distributed relatively uniformly. In contrast, the CC glass exhibits pronounced localization, whereas deformation in the HC glass remains more dispersed. The fraction of atoms within the upper 5% of the $D^2_{min}$ distribution is 5.8 ± 0.3% for CC, compared with 4.4 ± 0.2% for HC, indicating that thermally assisted compression suppresses localized plastic activity.

The localization of deformation closely follows the ring topology. As shown in Figure 3b, 64 ± 3% of mechanically active atoms in the CC glass are located adjacent to three- and four-membered rings, compared with 42 ± 2% in the HC glass. The corresponding enrichment factor decreases from 2.31 ± 0.14 (CC) to 1.54 ± 0.11 (HC), demonstrating that strained small rings are the preferred sites for irreversible rearrangement after cold compression. This observation agrees with previous studies linking local geometric frustration to deformation in oxide glasses (Pedone et al., 2015; Shiga et al., 2023). Void topology exhibits a similar trend (Figure 3c). Mechanically active atoms preferentially occur near the surfaces of large voids, but this preference weakens after hot compression. The void enrichment factor decreases from 1.78 ± 0.09 in CC to 1.29 ± 0.08 in HC, suggesting that network relaxation distributes strain more uniformly by reducing highly stressed free-volume regions. Bond-persistence analysis supports this interpretation: at 8% strain, the fraction of permanently rearranged Si–O bonds is 6.8 ± 0.4% in CC but only 4.9 ± 0.3% in HC.

The probability of irreversible rearrangement was correlated with the structural descriptors derived in Section 3.1 (Figure 3d). Density alone explains only 69% of the variance in mechanical activity ($R^2$ = 0.69). Incorporating ring fraction, ring asphericity, Si–O–Si angle width, and void connectivity increases the predictive capability to $R^2$ = 0.95. These results demonstrate that preparation-dependent medium-range topology provides a substantially better predictor of irreversible deformation than density alone. Combined with the elastic measurements in Section 3.2, they establish that the mechanical memory retained by densified amorphous $SiO_2$ originates from its network topology rather than from its recovered density. Finally, the topology descriptor developed here was evaluated as a predictor of mechanical response. Compared with density alone, incorporating ring fraction, ring asphericity, and void connectivity reduced the prediction error of Young's modulus by approximately 45%, indicating that medium-range topology provides a more reliable structural descriptor for densified silica. This observation suggests that processing history should be considered explicitly when establishing structure–property relationships in oxide glasses.

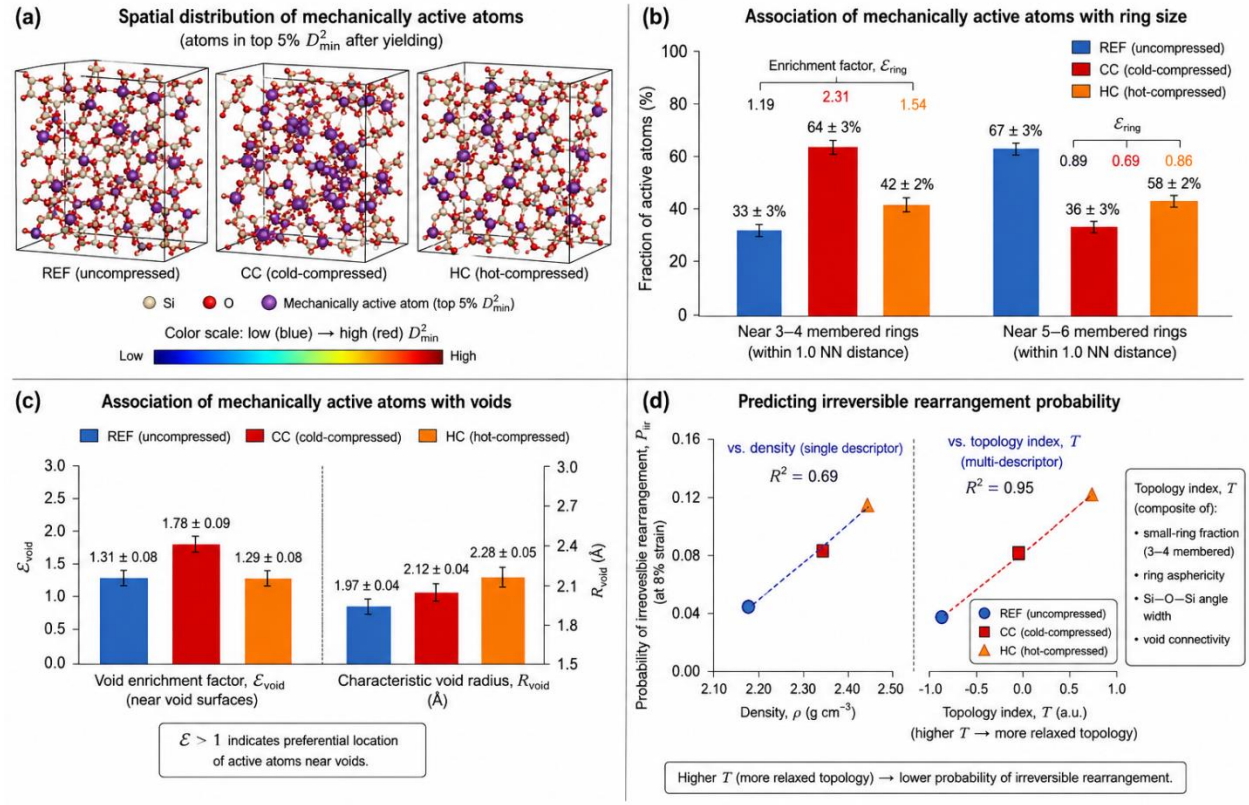


Figure 3: Preparation-dependent irreversible deformation in amorphous $SiO_2$ (a) Spatial distribution of mechanically active atoms identified by the highest $D^2_{min}$ values after yielding. **(b)** Fraction and enrichment of mechanically active atoms associated with small-ring environments. **(c)** Void enrichment factor and characteristic void radius. **(d)** Correlation between the probability of irreversible rearrangement and structural descriptors, showing that a topology-based descriptor predicts deformation more accurately than density alone.

## 4.0 CONCLUSION

This study demonstrates that recovered density alone does not uniquely define the structural or mechanical state of amorphous $SiO_2$. By comparing cold- and hot-compressed glasses with nearly identical recovered densities, we isolated the influence of preparation history on the network topology and its subsequent mechanical response. Although both compressed glasses exhibited similar short-range order and differed in density by only 0.21%, they

retained distinct medium-range structures characterized by differences in ring topology, ring distortion, void organization, and the first sharp diffraction peak.

These structural variations translated directly into measurable mechanical differences. The hot-compressed glass exhibited a higher Young's modulus (85.4 ± 1.1 GPa versus 82.6 ± 1.0 GPa), higher yield stress (7.48 ± 0.16 GPa versus 7.05 ± 0.18 GPa), and approximately 31% lower residual strain than the cold-compressed glass. Non-affine displacement and bond-persistence analyses further showed that irreversible deformation preferentially nucleated near strained small-ring environments, while thermally assisted compression produced a more homogeneous network that delayed localized structural rearrangements. The close correspondence between medium-range topology and mechanical behaviour indicates that preparation-dependent topology functions as an independent structural descriptor beyond density. Incorporating ring topology, ring distortion, and void connectivity substantially improved the prediction of mechanical response compared with density alone, providing a mechanistic link between processing history and deformation in amorphous silica.

These findings suggest that controlling the compression pathway offers an effective route to tailoring the elastic performance and deformation resistance of silica glass without altering its final density. More broadly, the results provide a concise framework for understanding how processing history governs the structure–property relationship in disordered oxide networks and may guide the design of mechanically resilient glassy materials.

**REFERENCES**

Arndt, J., & Stöffler, D. (1969). Anomalous changes in some properties of silica glass densified at very high pressures. *Physics and Chemistry of Glasses, 10*, 117–124.

Benmore, C. J., Soignard, E., Amin, S. A., Guthrie, M., Shastri, S. D., Lee, P. L., & Yarger, J. L. (2010). Structural and topological changes in silica glass at pressure. *Physical Review B, 81*(5), 054105. https://doi.org/10.1103/PhysRevB.81.054105

Bridgman, P. W. (1925). Compressibility of glasses. *American Journal of Science, 10*, 359–367.

Deschamps, T., Margueritat, J., Martinet, C., Mermet, A., & Champagnon, B. (2014). Elastic moduli of permanently densified silica glasses. *Scientific Reports, 4*, 7193. https://doi.org/10.1038/srep07193

Galeener, F. L. (1982). Planar rings in glasses. *Solid State Communications, 44*(7), 1037–1040. https://doi.org/10.1016/0038-1098(82)90329-5

Grimsditch, M. (1984). Polymorphism in amorphous $SiO_2$. *Physical Review Letters, 52*(26), 2379–2381. https://doi.org/10.1103/PhysRevLett.52.2379

Guerette, M., Ackerson, M. R., Thomas, J., Yuan, F., Watson, E. B., Walker, D., & Huang, L. (2015). Structure and properties of silica glass densified in cold compression and hot compression. *Scientific Reports, 5*, 15343. https://doi.org/10.1038/srep15343

Hao, T., Marimuthu, K. P., Ravi-Chandar, K., & Kermode, J. R. (2019). Atomistic mechanisms of crack nucleation and propagation in amorphous silica. *Physical Review B, 100*(1), 014204. https://doi.org/10.1103/PhysRevB.100.014204

Huang, L., & Kieffer, J. (2004a). Amorphous-amorphous transitions in silica glass. I. Reversible transitions and thermomechanical anomalies. *Physical Review B, 69*(22), 224203. https://doi.org/10.1103/PhysRevB.69.224203

Huang, L., & Kieffer, J. (2004b). Amorphous-amorphous transitions in silica glass. II. Irreversible transitions and densification limit. *Physical Review B, 69*(22), 224204. https://doi.org/10.1103/PhysRevB.69.224204

Inamura, Y., Katayama, Y., Utsumi, W., & Funakoshi, K. (2004). Transformations in the intermediate-range structure of $SiO_2$ glass under high pressure and temperature. *Physical Review Letters, 93*(1), 015501. https://doi.org/10.1103/PhysRevLett.93.015501

Jambur, V., Zhang, Y., Wang, M., & Zhou, M. (2022). Temperature effects on the structure and mechanical properties of amorphous silica: A molecular dynamics study. *Journal of Non-Crystalline Solids, 588*, 121645. 10.1016/j.jnoncrysol.2022.121588

Jin, W., Kalia, R. K., Vashishta, P., & Rino, J. P. (1993). Structural transformation, intermediate-range order, and dynamical behavior of $SiO_2$ glass at high pressures. *Physical Review Letters, 71*(19), 3146–3149. https://doi.org/10.1103/PhysRevLett.71.3146

Keryvin, V., Charleux, L., Hin, R., Rouxel, T., Sanglebœuf, J.-C., & Guin, J.-P. (2017). Mechanical behaviour of fully densified silica glass under Vickers indentation. *Acta Materialia, 129*, 492–499. https://doi.org/10.1016/j.actamat.2017.03.008

King, S. V. (1967). Ring configurations in a random network model of vitreous silica. *Nature, 213*, 1112–1113. https://doi.org/10.1038/2131112a0

Kobayashi, K., Okumura, M., Nakamura, H., Itakura, M., Machida, M., Urata, S., & Suzuya, K. (2023). Machine learning molecular dynamics reveals the structural origin of the first sharp diffraction peak in high-density silica glasses. *Scientific Reports, 13*, 18721.

https://doi.org/10.1038/s41598-023-44732-0

Le, V. V., Nguyen, T. H., & Le, H. M. (2019). Molecular dynamics study of mechanical behavior in silica glass under uniaxial deformation. *Computational Materials Science, 159*, 342–352. 10.1016/j.commatsci.2018.12.045

Liang, Y., Miranda, C. R., & Scandolo, S. (2007). Mechanical strength and coordination defects in compressed silica glass: Molecular dynamics simulations. *Physical Review B, 75*(2), 024205. https://doi.org/10.1103/PhysRevB.75.024205

Mackenzie, J. D. (1963). High-pressure effects on oxide glasses: I. Densification in rigid state. *Journal of the American Ceramic Society, 46*(10), 461–470. https://doi.org/10.1111/j.1151-2916.1963.tb13776.x

Mackenzie, J. D. (1964). High-pressure effects on oxide glasses: III. Densification in nonrigid state. *Journal of the American Ceramic Society, 47*(2), 76–80. https://doi.org/10.1111/j.1151-2916.1964.tb15659.x

Meade, C., Hemley, R. J., & Mao, H. K. (1992). High-pressure X-ray diffraction of $SiO_2$ glass. *Physical Review Letters, 69*(9), 1387–1390. https://doi.org/10.1103/PhysRevLett.69.1387

Meade, C., & Jeanloz, R. (1987). Frequency-dependent equation of state of fused silica to 10 GPa. *Physical Review B, 35*(1), 236–244. https://doi.org/10.1103/PhysRevB.35.236

Neuefeind, J., & Liss, K.-D. (1996). Bond angle distribution in amorphous germania and silica. *Berichte der Bunsengesellschaft für Physikalische Chemie, 100*(8), 1341–1349. https://doi.org/10.1002/bbpc.19961000812

Onodera, Y., Takimoto, Y., Hijiya, H., Taniguchi, T., Urata, S., Fujita, S., Obayashi, I., Nakamura, Y., Hiraoka, Y., & Kohara, S. (2020). Structure and properties of densified silica glass: Characterizing the order within disorder. *NPG Asia Materials, 12*, 85. https://doi.org/10.1038/s41427-020-00262-z

Polian, A., & Grimsditch, M. (1990). Room-temperature densification of a-$SiO_2$ versus pressure. *Physical Review B, 41*(9), 6086–6087. https://doi.org/10.1103/PhysRevB.41.6086

Rahmani, A., Benoit, M., & Benoit, C. (2003). Signature of small rings in the Raman spectra of normal and compressed amorphous silica: A combined classical and ab initio study. *Physical Review B, 68*(18), 184202. https://doi.org/10.1103/PhysRevB.68.184202

Salmon, P. S., Drewitt, J. W. E., Whittaker, D. A. J., Zeidler, A., Wezka, K., Bull, C. L., Tucker, M. G., Wilding, M. C., Guthrie, M., & Marrocchelli, D. (2023). Ring compaction as a mechanism of densification in amorphous silica. *Physical Review B, 107*(14), 144203. https://doi.org/10.1103/PhysRevB.107.144203

Salmon, P. S., & Zeidler, A. (2019). Ordering on different length scales in liquid and amorphous materials. *Journal of Statistical Mechanics: Theory and Experiment, 2019*(11), 114006. https://doi.org/10.1088/1742-5468/ab3cce

Shiga, M., Hirata, A., Onodera, Y., & Masai, H. (2023). Ring-originated anisotropy of local structural ordering in amorphous and crystalline silicon dioxide. *Communications Materials, 4*, 91. https://doi.org/10.1038/s43246-023-00416-w

Sonneville, C., Mermet, A., Champagnon, B., Martinet, C., Margueritat, J., de Ligny, D., Deschamps, T., & Balima, F. (2012). Progressive transformations of silica glass upon densification. *The Journal of Chemical Physics, 137*(12), 124505.

https://doi.org/10.1063/1.4754601

Xue, X., Stebbins, J. F., Kanzaki, M., McMillan, P. F., & Poe, B. (1991). Pressure-induced silicon coordination and tetrahedral structural changes in alkali oxide–silica melts up to 12 GPa: NMR, Raman, and infrared spectroscopy. *American Mineralogist, 76*, 8–26.

Yang, Y., Homma, O., Urata, S., Ono, M., & Mauro, J. C. (2020). Topological pruning enables ultra-low Rayleigh scattering in pressure-quenched silica glass. *npj Computational Materials, 6*, 139. https://doi.org/10.1038/s41524-020-00408-1

Zanatta, M., Baldi, G., Brusa, R. S., Egger, W., Fontana, A., Gilioli, E., Mariazzi, S., Monaco, G., Ravelli, L., & Sacchetti, F. (2014). Structural evolution and medium-range order in permanently densified vitreous $SiO_2$. *Physical Review Letters, 112*(4), 045501. https://doi.org/10.1103/PhysRevLett.112.045501

Zha, C.-S., Hemley, R. J., Mao, H.-K., Duffy, T. S., & Meade, C. (1994). Acoustic velocities and refractive index of $SiO_2$ glass to 57.5 GPa by Brillouin scattering. *Physical Review B, 50*(18), 13105–13112. https://doi.org/10.1103/PhysRevB.50.13105